Efficiency Comparison of Wavelet Packet and Adapted Local Cosine Bases for Compression of a Two-dimensional Turbulent Flow

Mladen Victor Wickerhauser* Marie Farge† Eric Goirand*
Eva Wesfreid‡ Echeyde Cubillo§

June 2, 1994

Abstract

We compare the efficiency of two rank-reduction methods for representing the essential features of a two-dimensional turbulent vorticity field. The two methods are both projections onto the largest components, in one case onto the wavelet packet best basis, in the other case onto the best basis of adapted local cosines. We compare the two methods in three ways: for efficiency of capturing enstrophy or square-vorticity, for faithfulness to the power spectrum, and for precision in resolving coherent structures. These properties are needed for subsequent segmentation into isolated coherent structures, or for measurement of statistical quantities related to coherent structures. We find that in all three respects the wavelet packet representation is superior to the local cosine representation.

1 Background

1.1 Models of turbulence

The classical approach to turbulent flows considers either ensemble averages or equivalently, assuming ergodicity, time or space averages. In particular the Kraichnan–Batchelor theory for two-dimensional turbulence [2, 10] postulates

*Mathematics Department, Washington University, St. Louis, Missouri, USA

†Laboratoire de Metéorologie Dynamique du CNRS, Ecole Normale Supèrieure, 24 rue Lhomond, 75231 Paris Cedex 5, France

‡CEREMADE, Université Paris–Dauphine, 2, place du Maréchal de Lattre de Tassigny, 75775 Paris, France

§Center for Theoretical Studies of Physical Systems, Clark Atlanta University, Atlanta, Georgia 30314, USA

homogeneous mixing within the flow and supposes that the whole vorticity field is involved in the turbulent cascade process.

In contrast to this approach, we think that a two-dimensional turbulent flow is generically inhomogeneous and can be better described as a superposition of coherent rotational vortices embedded in a random quasi-irrotational flow. We have observed, in numerical simulations of two-dimensional Navier–Stokes equations with random initial conditions, that isolated vortices result from the condensation of enstrophy into localized, well-separated structures. These structures are stable as long as they do not interact with one another, but during close encounters they experience strong deformations, which then excite some internal degrees of freedom. This gives rise to a local *cascade* or transfer of enstrophy toward small scales and to its concomitant dissipation. Consequently, only a limited *active portion* of the vorticity field, correlated to the coherent vortices, is responsible for the turbulent cascade. The remainder, or *background portion* of the field, is passively advected and plays a negligible dynamical role.

Our *atomic* view may be compared with the vortex methods of Winckelmans and Leonard [22], Marchioro and Pulvirenti [15], and Saffman [18]. We generalize the simplest model used to approximate two-dimensional flows, that of superposed *point vortices*, by considering the flow to be a superposition of *atoms* that we choose from among a library of smooth localized functions such as wavelet packets [4] or localized cosine functions [3, 14]. The additional parameters available to these atoms enable us to take into account the internal degrees of freedom of each vortex, which can be considered as a *molecule*.

1.2 Turbulent flow computation

The usual methodology to compute turbulent flow evolutions is to separate them into active components responsible for the nonlinear and chaotic dynamics, and passive components, advected by the active ones which they merely perturb. The active components must be explicitly computed, while the passive components can be modeled by some subgrid scale parametrization. The question we want to address is: which components in a two-dimensional turbulent flow are active and which are passive?

1.2.1 Wavenumber segmentation

The commonly used computational techniques, such as Galerkin methods, large eddy simulation, and nonlinear Galerkin methods, assume that there exists a gap in the energy spectrum of turbulent flows. Such a gap allows us unequivocally to distinguish low-wavenumber Fourier modes, which we consider to be active, from high-wavenumber Fourier modes, which we consider to be passive. In fact this assumption is misleading, because such a spectral gap is never observed, neither for two-dimensional turbulent flows, nor for three-dimensional ones. We have to look for other functional bases where some kind of gap both exists and

represents a physically meaningful distinction. Then the segmentation between active and passive modes will be more than a leap of faith.

In the case of three-dimensional turbulence, according to Kolmogorov's theory [9, 17], energy cascades directly from low wavenumbers to high wavenumbers, where it is dissipated. In this case, the previous wavenumber segmentation is still relevant as long as there is no local inverse energy cascade from high-wavenumbers to low-wavenumbers. But in fact, such an inverse cascade seems to arise whenever the flow presents well-localized active structures, such as horseshoe vortices in boundary or mixing layers.

In the case of two-dimensional turbulence, wavenumber segmentation is always inappropriate. Kraichnan's theory [11, 12] predicts, and numerical experiments have confirmed, that two-dimensional turbulent flows on average exhibit inverse energy cascades. Furthermore, any segmentation must also take into account the presence of coherent structures, since they are generic in two-dimensional turbulence and their mutual interactions are very probably responsible for the inverse energy cascade. Because such features are well localized in physical space, we propose to segment the field into components with definite physical space location as well as recognizable spectral content.

1.2.2 Phase space segmentation

The method we will follow to define a better segmentation is to search for a decomposition which puts the strongest concentration of enstrophy into the fewest *phase space atoms*. We choose the atoms to be smooth functions, well localized in both space and wavenumber coordinates. The additional dimensions available in phase space better allow us to discriminate individual coherent structures. We propose to characterize a coherent structure as the superposition of phase space atoms which share the same position. The degrees of freedom within each coherent structure are just the amplitudes of its component atoms.

We isolate structures by *coarse graining* in phase space. This is most easily accomplished if our representation yields very few large components, rather than large numbers of smaller components. We therefore compare techniques on the basis of their gain of concentration. This is similar to the goal of adapted waveform denoising [5], or else transform coding image compression [19, 21], where effectiveness is measured by transform coding gain. In this paper we will compare transform coding into wavelet packets and local cosine phase space atoms. The wavelet packet representation has proved superior to the Fourier representation in capturing features which control the dynamics of two-dimensional flow evolution [7].

2 Methods

2.1 Two-dimensional incompressible viscous flows

We begin with a high resolution direct numerical solution of the Navier–Stokes equations, which describe the dynamics of a two-dimensional incompressible viscous flow. In the periodic plane $S = (0, 2\pi) \times (0, 2\pi) \subset \mathbf{R}^2$ and in the absence of external forcing, these take the following form:

$$\begin{aligned} \frac{\partial \mathbf{u}}{\partial t} + (\mathbf{u} \cdot \nabla)\mathbf{u} + \nabla P - \nu \nabla^2 \mathbf{u} = 0, &\qquad \text{in } S \times \mathbf{R}^+, \\ \nabla \cdot \mathbf{u} = 0, &\qquad \text{in } S \times \mathbf{R}^+, \\ \mathbf{u}(\mathbf{x}, 0) = \mathbf{u}_0(\mathbf{x}), &\qquad \text{in } S. \end{aligned}$$

Here $\mathbf{u}$ is the velocity field, P is the pressure field, and ν is the kinematic viscosity. We also impose periodic boundary conditions. We can rewrite these equations in terms of *vorticity* ω and *streamfunction* ψ, defined by

$$\mathbf{u} = \begin{pmatrix} u_1 \\ u_2 \end{pmatrix} = \begin{pmatrix} -\frac{\partial \psi}{\partial x_2} \\ \frac{\partial \psi}{\partial x_1} \end{pmatrix}; \qquad \omega = \frac{\partial u_2}{\partial x_1} - \frac{\partial u_1}{\partial x_2}.$$

The Navier–Stokes equations then become

$$\begin{aligned} \frac{\partial \omega}{\partial t} + J(\psi, \omega) - \nu \nabla^2 \omega = 0, &\qquad (\mathbf{x}, t) \in S \times \mathbf{R}^+; \\ \omega = \nabla^2 \psi, &\qquad (\mathbf{x}, t) \in S \times \mathbf{R}^+; \\ \omega(\mathbf{x}, 0) = \omega_0(\mathbf{x}), &\qquad \mathbf{x} \in S. \end{aligned}$$

Again we have periodic boundary conditions. The Jacobian operator in terms of these new variables is:

$$J(\psi, \omega) = \frac{\partial \psi}{\partial x_1}\frac{\partial \omega}{\partial x_2} - \frac{\partial \psi}{\partial x_2}\frac{\partial \omega}{\partial x_1}.$$

We can expand ω and ψ in their Fourier series over the periodic domain S:

$$\begin{aligned} \omega(\mathbf{x}, t) = \sum_{\mathbf{k}} \hat{\omega}(\mathbf{k}, t) e^{i\mathbf{k}\cdot\mathbf{x}}, &\qquad \hat{\omega}(\mathbf{k}, t) = \frac{1}{2\pi} \int_{\mathbf{x} \in S} \omega(\mathbf{x}, t) e^{-i\mathbf{k}\cdot\mathbf{x}} \, d\mathbf{x}; \\ \psi(\mathbf{x}, t) = \sum_{\mathbf{k}} \hat{\psi}(\mathbf{k}, t) e^{i\mathbf{k}\cdot\mathbf{x}}, &\qquad \hat{\psi}(\mathbf{k}, t) = \frac{1}{2\pi} \int_{\mathbf{x} \in S} \psi(\mathbf{x}, t) e^{-i\mathbf{k}\cdot\mathbf{x}} \, d\mathbf{x}. \end{aligned}$$

We obtain a turbulent vorticity field by starting with a random initial vorticity field $\omega_0(\mathbf{x})$, then integrating for many time steps in the presence of time-periodic external forcing. Forcing is subsequently turned off and the same integration is continued until the vorticity field reaches a statistically steady state.

To integrate the Navier–Stokes equations, we use a pseudospectral Galerkin method which, at each time step, performs all differentiation in $\hat{\omega}, \hat{\psi}$ coordinates and all multiplication in ω, ψ coordinates. Both ω and ψ are represented as finite Fourier series, or superpositions of the Fourier modes at wavenumbers $0 \leq |\mathbf{k}| < k_r$, where k_r is the cutoff wavenumber which gives some fixed resolution. The time integration is done using an Adams–Bashforth scheme. For the subgrid scale model we use a hyperdissipation operator $-(-\nabla^2)^4$, which replaces the Laplacian operator in the Navier–Stokes equations.

The periodic plane S is sampled on 512^2 grid points in our simulation. The program ran for 38,000 time steps $\Delta t = 10^{-3}$ in units of T^1, which corresponds to 635 initial eddy-turnover times, starting from a random distribution of vorticity with energy $E = 0.5$ in ML^2T^{-2} units and an initial enstrophy $Z = 279$ in T^{-2} units. The vorticity field we analyze is one time slice, presumably a typical snapshot of a fully-developed turbulent flow, taken from the equilibrium end of this preparation.

2.2 Wavelet packet best basis

Wavelet packets are generalizations of the compactly-supported wavelets introduced by Daubechies, Mallat, and Meyer [6, 13, 16]. They constitute an overabundant set of basis functions with remarkable orthogonality properties, namely, that very many subsets form orthonormal bases. The one-dimensional functions were first described in Reference [4]. Each basis element ψ is characterized by three attributes: scale s, wavenumber k, and position p, so we may label them ψ_{skp}. By the Heisenberg uncertainty principle, it is not possible to localize a function to arbitrary precision in both p and k; we must have $\delta p \cdot \delta k \geq 1$ in normalized units, where δp is the uncertainty in position and δk is the uncertainty in wavenumber. In our construction, we have $\delta p \approx 2^s$ and $\delta k \approx 2^{-s}$ in the same normalization, so that the product of the uncertainties is roughly as small as possible. Such functions, which cannot be significantly better localized in phase space, are evidently phase space atoms.

Fourier analysis with such waveforms or atoms consists of calculating the *wavelet packet transform* $w_{skp}(f) = \langle \psi_{skp}, f \rangle$. Certain subsets of the indices (s, k, p) give orthonormal bases B, and for these subsets we have the inversion formula:

$$f = \sum_{(s,k,p) \in B} \langle \psi_{skp}, f \rangle \psi_{skp}.$$

Wavelet packets are rarely constructed explicitly. More usually, we simply apply the fast discrete algorithm described in Reference [4] to the sampled values of f, and thereby produce the coefficients $w_{skp}(f)$. The underlying functions ψ can, however, be developed as follows. We introduce two (short) finite sequences

n	Low-pass filter coefficient h_n	High-pass filter coefficient g_n
< 0	0	0
0	$1.6387336463179785 \times 10^{-2}$	$-7.2054944536811512 \times 10^{-4}$
1	$-4.1464936781966485 \times 10^{-2}$	$1.8232088709100992 \times 10^{-3}$
2	$-6.7372554722299874 \times 10^{-2}$	$5.6114348193659885 \times 10^{-3}$
3	$3.8611006682309290 \times 10^{-1}$	$-2.3680171946876750 \times 10^{-2}$
4	$8.1272363544960613 \times 10^{-1}$	$-5.9434418646471240 \times 10^{-2}$
5	$4.1700518442377760 \times 10^{-1}$	$7.6488599078264594 \times 10^{-2}$
6	$-7.6488599078264594 \times 10^{-2}$	$4.1700518442377760 \times 10^{-1}$
7	$-5.9434418646471240 \times 10^{-2}$	$-8.1272363544960613 \times 10^{-1}$
8	$2.3680171946876750 \times 10^{-2}$	$3.8611006682309290 \times 10^{-1}$
9	$5.6114348193659885 \times 10^{-3}$	$6.7372554722299874 \times 10^{-2}$
10	$-1.8232088709100992 \times 10^{-3}$	$-4.1464936781966485 \times 10^{-2}$
11	$-7.2054944536811512 \times 10^{-4}$	$-1.6387336463179785 \times 10^{-2}$
> 11	0	0

Table 1: C 12 coefficients for orthogonal wavelet packets

$\{h_n\}$ and $\{g_n\}$, called *conjugate quadrature filters*, which satisfy the relations:

$$\sum_n h_{2n} = \sum_n h_{2n+1} = \frac{1}{\sqrt{2}}, \qquad g_n = -(-1)^n h_{11-n}, \qquad \text{for all } n; \tag{1}$$

$$\sum_n h_n h_{n+2m} = \sum_n g_n g_{n+2m} = \begin{cases} 1, & \text{if } m = 0, \\ 0, & \text{otherwise;} \end{cases} \tag{2}$$

$$\sum_n h_n g_{n+2m} = 0, \qquad \text{for all } m \in \mathbf{Z}. \tag{3}$$

Next, we define a family of functions recursively for integers $k \geq 0$ by:

$$W_{2k}(x) = \sqrt{2} \sum_n h_n W_k(2x - n); \quad W_{2k+1}(x) = \sqrt{2} \sum_n g_n W_k(2x - n) \tag{4}$$

Note that W_0 satisfies a fixed-point equation. Conditions 1 through 3 ensure that a unique solution to this fixed-point problem exists, and that $\{W_k : k \in \mathbf{Z}\}$ forms an orthonormal basis for $L^2(\mathbf{R})$. The quadrature filter pair h, g can be chosen (see Reference [6]) so that the solution has any prescribed degree of smoothness.

Equations 1 through 4 all have periodic analogs as well, which we use in the case of periodic boundary conditions. For the experiments in this article, we used periodic algorithm with the so-called "C 12" coefficients, using h_n and g_n as given in Table 1.

One-dimensional wavelet packets are defined from these W_k by the formula:

$$\psi_{skp}(x) = 2^{-s/2} W_k(2^{-s}x - p).$$

As described in Reference [4], we obtain an orthonormal basis subset $\mathcal{I}$ by taking those functions $\{\psi_{skp} : (s,k,p) \in \mathcal{I}\}$ for which the half-open *dyadic intervals* $\{[\frac{k}{2^s}, \frac{k+1}{2^s}) : (s,k,p) \in \mathcal{I}\}$ form a disjoint cover of the unit interval.

Our library of basis functions in two dimensions consists of all possible tensor products of the ψ functions with both factors sharing the same scale s. The definitions and formulas for this two-dimensional case may be found in Reference [21], elsewhere in this volume. Certain basis subsets can be described by disjoint tilings of the unit square, as follows. Let I be a half-open *dyadic square* $[\frac{k_x}{2^s}, \frac{k_x+1}{2^s}) \times [\frac{k_y}{2^s}, \frac{k_y+1}{2^s})$ and put $\psi_{I,(p_x,p_y)}(x,y) = 2^{-s} s W_{k_x}(2^{-s}x - p_x) W_{k_y}(2^{-s}y - p_y)$. Then every basis in our library, for functions on the $2^S \times 2^S$ grid, corresponds to a set of the form:

$$\{\psi_{I,(p_x,p_y)} : I \in \mathcal{I}, p_x \in \mathbf{Z}, p_y \in \mathbf{Z}, 0 \le p_x < 2^{S-s}, 0 \le p_y < 2^{S-s}\},$$

where $\mathcal{I}$ is a disjoint cover of the unit square by such dyadic squares I, for $0 \le s \le S$ and $0 \le k_x, k_y < 2^{s-1}$. Computation of inner products with all such functions is performed recursively, as is the search for the best-basis; the implementation of both algorithms is described in Reference [20]. The entire procedure has complexity $O(N \log N)$ where N is the rank of the problem, and $N = 2^{2S}$ for the original grid-point formulation.

The *best basis* of wavelet packets for a fixed vorticity field is the one maximizing the coding gain or *entropy*, as described in Reference [21]. The field is then approximated by ω^ϵ, a superposition of just the largest components. Call the best basis $\mathcal{I}_*$. We project onto the top few coefficients as follows:

$$\omega^\epsilon = \sum_{|c_I| > \epsilon} c_I \psi_I .$$

Here $I \in \mathcal{I}_*$, $c_I = \langle \omega, \psi_I \rangle$ and ϵ is some predetermined threshold. We also sum over all integer translates (p_x, p_y), even though that notation is suppressed for compactness.

In our four compression experiments, ϵ was chosen to ensure that ω^ϵ contained, 99.9, 99, 90, and 50 percent of the total *enstrophy* (or square vorticity) of the field. The remainder fields $\omega^r = \omega - \omega^\epsilon$ thus contain 0.1, 1, 10, and 50 percent of the enstrophy, respectively.

2.3 Local cosine best basis

The local cosine transform has much in common with the windowed Fourier transform [8], which is a well known decomposition into phase space atoms. Like the one-dimensional wavelet packet library, the library of one-dimensional local cosines contains atoms that can be characterized by scale s, wavenumber k, and position p. Since local cosines are real-valued, orthonormal analogs of windowed Fourier modes, we may use the nominal window width for s, the

nominal left endpoint of the window for p, and the frequency index for k. Local cosines have the formula

$$\psi_{skp}(x) = \sqrt{\frac{2}{2^s}}\; b(\frac{x-p}{2^s})\;\; \cos\left[\pi(k+\frac{1}{2})\frac{x-p}{2^s}\right].$$

Here $b = b(x)$ is a smooth function supported in the compact interval $[-\epsilon, 1+\epsilon]$ for $0 \le \epsilon < \frac{1}{2}$. This interval contains $[0,1]$ which we will say is its *nominal support*. The only special features are the use of odd half-integer frequencies in the cosine function, and the symmetry properties of the window function b:

$$b(-x)^2 + b(x)^2 = 1, \quad b(1-x)^2 + b(1+x)^2 = 1, \qquad -\epsilon < x < \epsilon.$$

These special properties insure orthogonality and make certain fast algorithms possible. Reference [1] explores the one-dimensional case in much greater detail.

Two-dimensional local cosines consist of tensor products $\psi_{skp}(x)\psi_{s'k'p'}(y)$, and their nominal supports are the cartesian product rectangles of the nominal supports of the x and y factors. For simplicity we will be using the same scale in both directions: $s = s'$ throughout this paper. Subsets of such functions can be indexed by dyadic squares, with the squares correspond to the nominal supports of the functions.

A two-dimensional *adapted local cosine basis*, as described in Reference [21] elsewhere in this volume, corresponds to a disjoint cover by dyadic squares. The *best basis* for a given vorticity field is the one which maximizes coding gain. Descriptions and basic implementations of the algorithm to extract this basis may be found in Reference [20].

2.4 Radial power spectrum

Given a sampled vorticity field $\omega(\mathbf{x}, t_0)$ at some instant t_0, we can compute its Fourier power spectrum $|\hat{\omega}(\mathbf{k}, t_0)|^2$ using the discrete Fourier transform or FFT. This will be a nonnegative function of two variables, but we are only interested in its mean behavior as $|\mathbf{k}| \to \infty$, regardless of direction. Thus, we will average over all rotations to get a *radial power spectrum density*:

$$\rho(k) = \frac{1}{2\pi k} \oint_{|\mathbf{k}|=k} |\hat{\omega}(\mathbf{k})|^2, \qquad k \ge 0.$$

We have suppressed the unneeded variable t_0. The *radial power spectrum* that we actually plot is an approximation of this density, found by summing the discrete samples of $|\hat{\omega}|^2$ lying in the annulus between two wavenumber radii k and $k+1$, then dividing by the multiplicity M_k or number of samples in each annulus:

$$\rho_{disc}(k) = \frac{1}{2\pi k\, M_k} \sum_{k \le |\mathbf{k}| < k+1} |\hat{\omega}(\mathbf{k})|^2, \qquad k = 0, 1, \ldots$$

The resolution of the discrete radial power spectrum is the same as that of the discrete Fourier transform.

From the slope of the log–log plot of ρ_{disc}, we can estimate the scaling law for enstrophy as a function of wavenumber. This can be used to test the faithfulness of segmentation methods, as described in Reference [7].

3 Results

We focused our attention on one vorticity field (Figure 1), representing what we believe is a generic time slice of a homogenous, isotropic, fully developed turbulent flow. Our experiment segmented it into high-enstrophy and low-enstrophy components in both the wavelet packet and local cosine best bases, and we reconstructed the different portions for visual inspection (Figures 2 to 5). We then computed the radial power spectra of the reconstructed pieces (Figures 6 to 8), and estimated the spectral slopes in the inertial and noise-like regions (Tables 2 and 3). Finally, we found the rate of accumulation of enstrophy by components in the two methods (Figure 9 and Table 4).

3.1 Strong fields reconstructed after compression

Analysis and synthesis, either with local cosines or wavelet packets, is a perfect reconstruction algorithm, but we envision discarding most of the components before synthesis so as to compress the representation. The disappearance of some components introduces distortion and artifacts that become progrssively more visible at higher compression rates.

In the local cosine case, the basis functions are registered on a fixed grid which may be inconveniently placed with respect to the principal features. Thus, it may take a superposition of several components to match the phase of a peak. If some of the components are small and disappear in the compression, there may be oscillations in the reconstructed compressed field near features of interest. These are visible in Figures 2b,d to 5b,d. Some of this oscillation also appears in the wavelet packet reconstructions in Figures 2a,c to 5a,c.

A *quasi-singular structure*, namely a sampled function near a discontinuity or cusp, is described as the superposition of all Fourier modes. The local cosine representation, like any Fourier compression, is unable to preserve nonsmooth functions. Thus the compressed image is undesirably smoother than the original, especially at high compression rates (Figure 3b,d). On the other hand, wavelet packets include wavelets which concentrate the energy of singularities into a few components. Those components vital for representing nonsmooth portions of the field survive the wavelet packet compression, so that even at high compression rates (Figure 3a,c) the quasi-singular features remain sharp and well-separated.

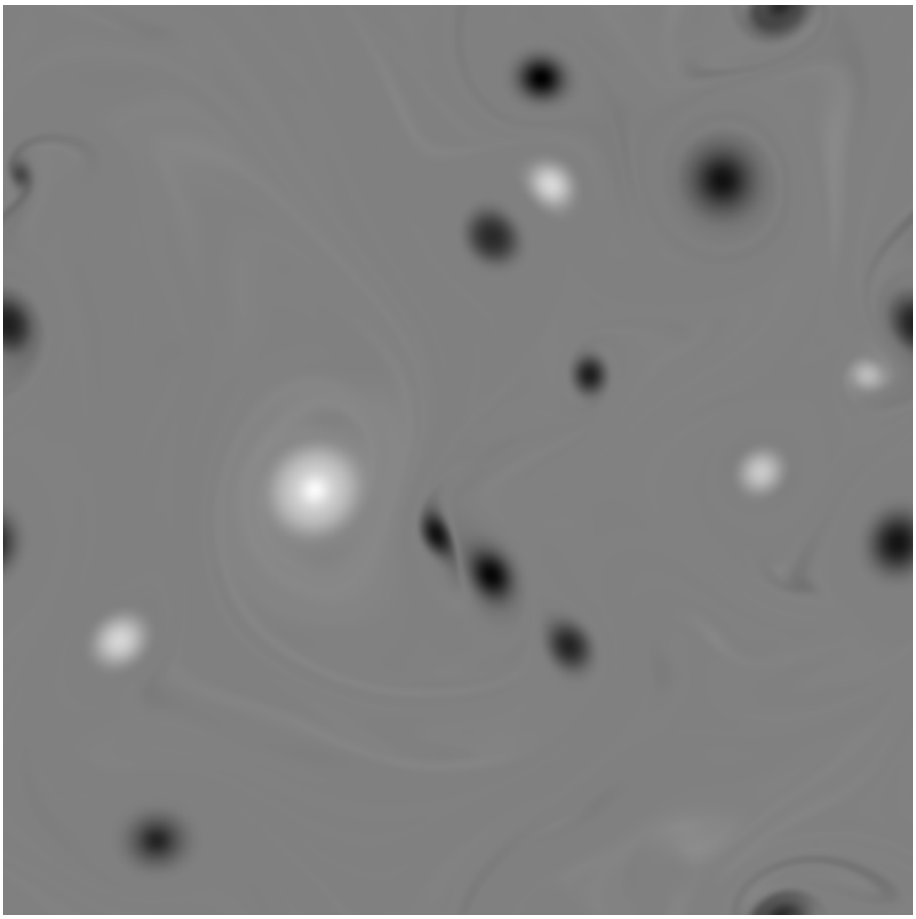

Figure 1: Vorticity field at an instant of time, scaled to fill an 8-bit dynamic range.

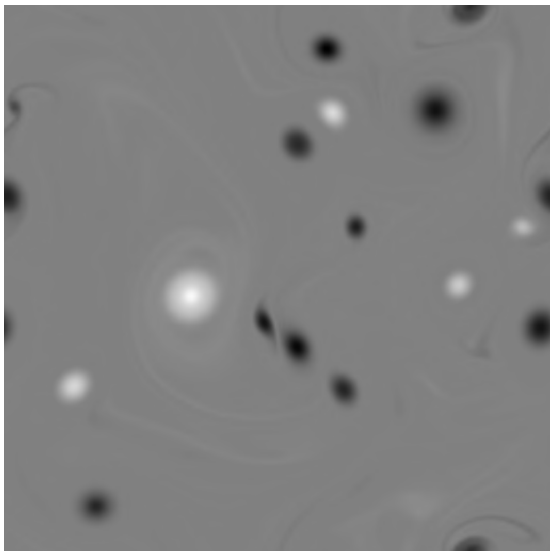

a. 3129 wavelet packets, $.999Z$.

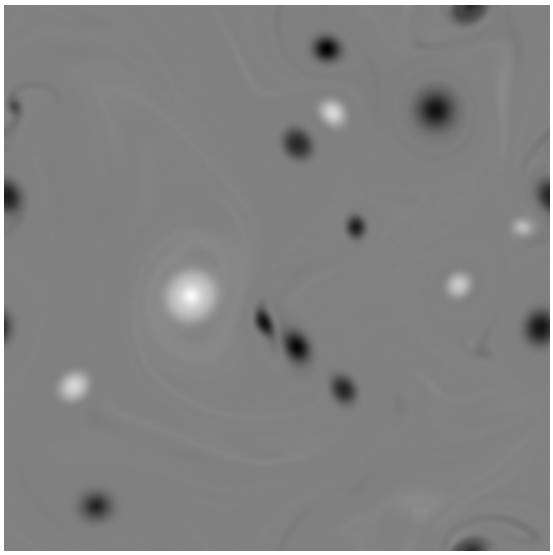

b. 5114 local cosines, $.999Z$.

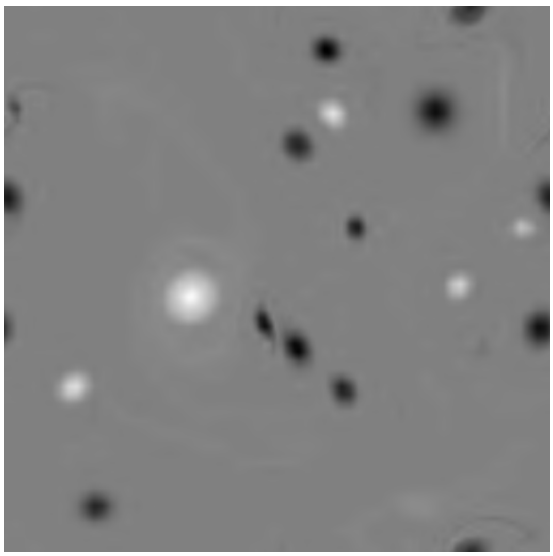

c. 803 wavelet packets, $.99Z$.

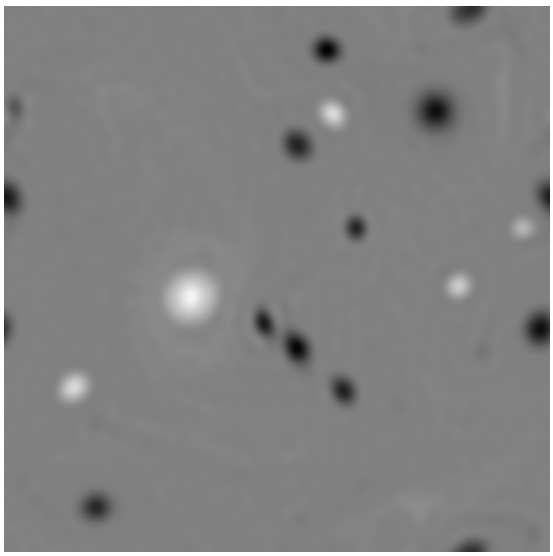

d. 1479 local cosines, $.99Z$.

Figure 2: Vorticity fields reconstructed from "many" strongest wavelet packets and local cosines, scaled to fill an 8-bit dynamic range.

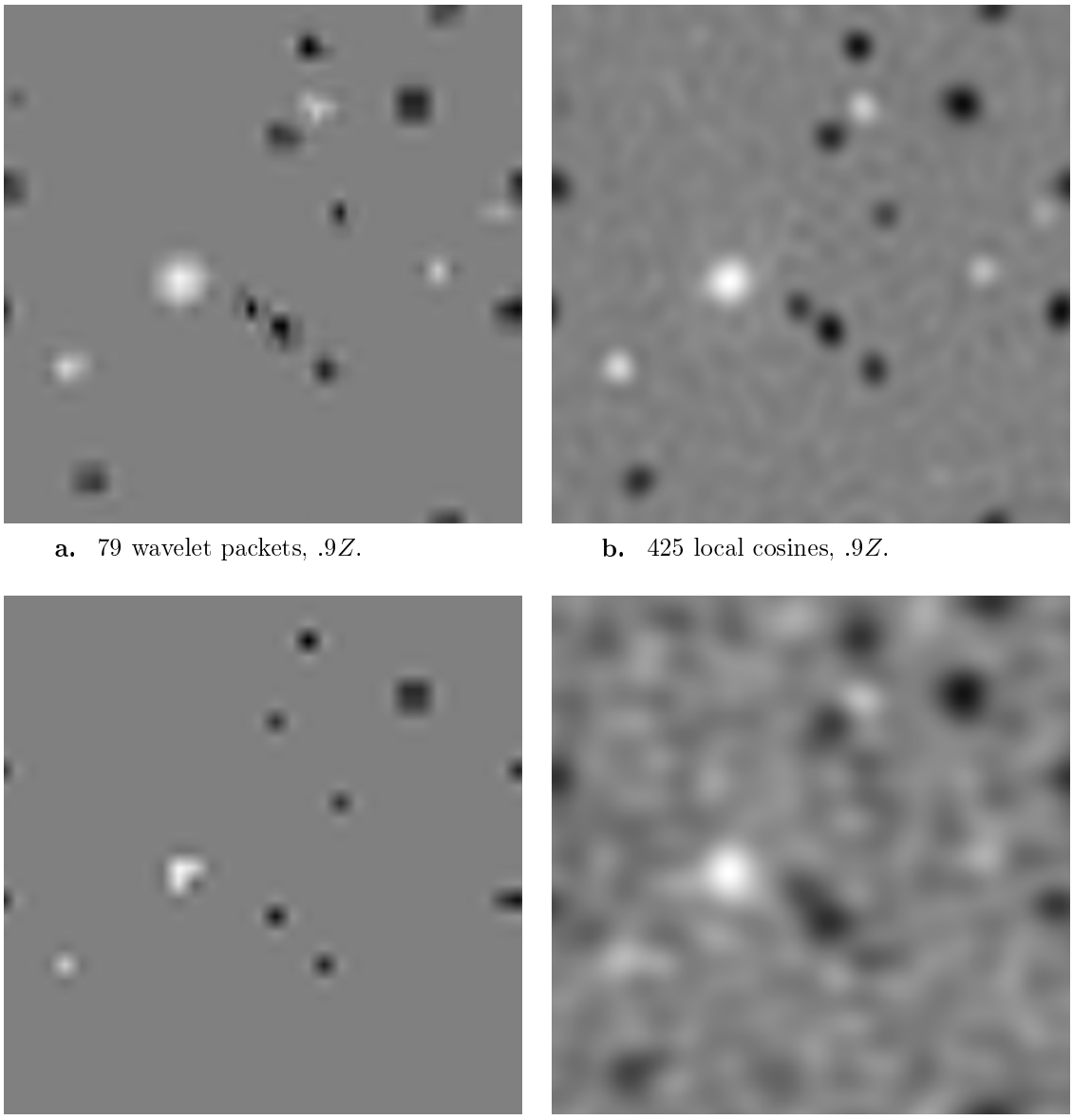

a. 79 wavelet packets, $.9Z$.

b. 425 local cosines, $.9Z$.

c. 16 wavelet packets, $.5Z$.

d. 70 local cosines, $.5Z$.

Figure 3: Vorticity fields reconstructed from "few" strongest wavelet packets and local cosines, scaled to fill an 8-bit dynamic range.

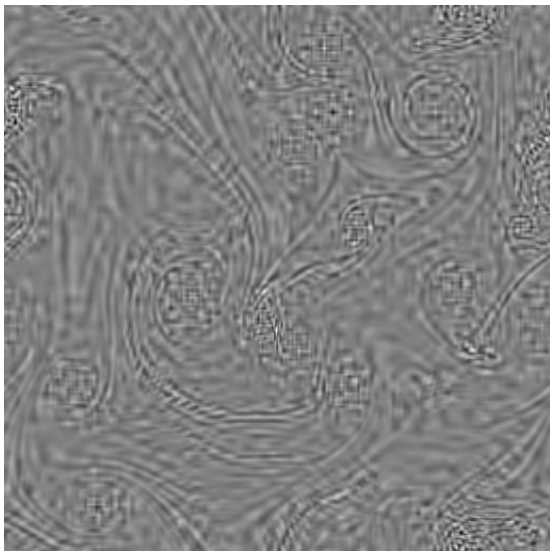

a. 259,015 wavelet packets, $.001Z$.

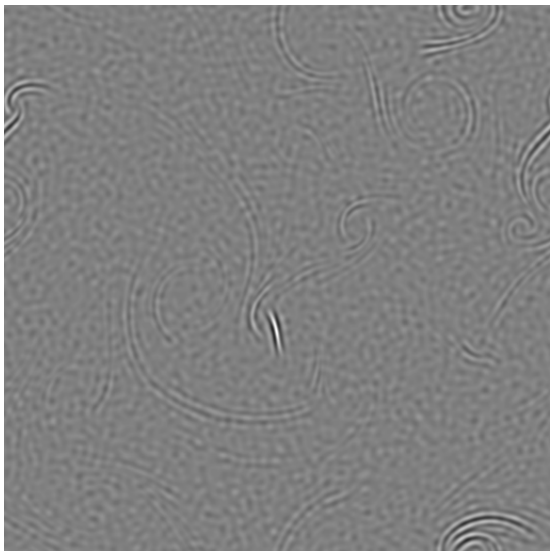

b. 257,030 local cosines, $.001Z$.

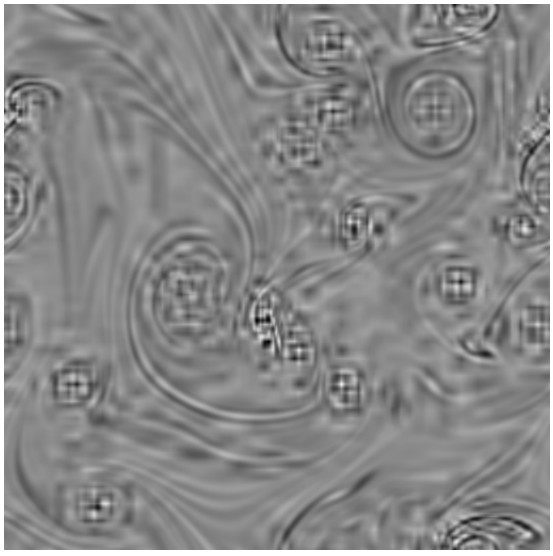

c. 261,341 wavelet packets, $.01Z$.

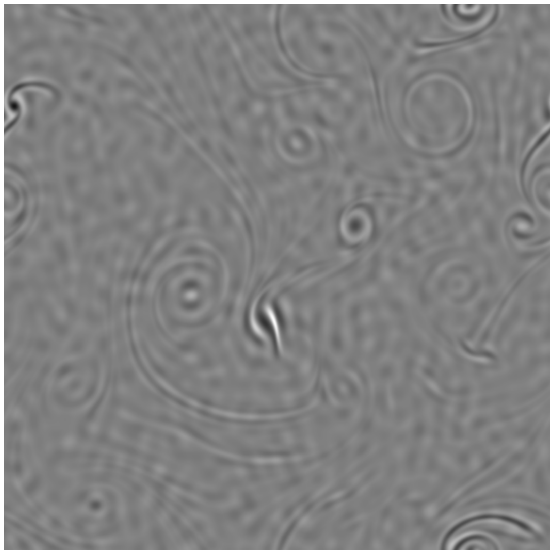

d. 260,665 local cosines, $.01Z$.

Figure 4: Vorticity fields reconstructed from "few" weakest wavelet packets and local cosines, scaled to fill an 8-bit dynamic range.

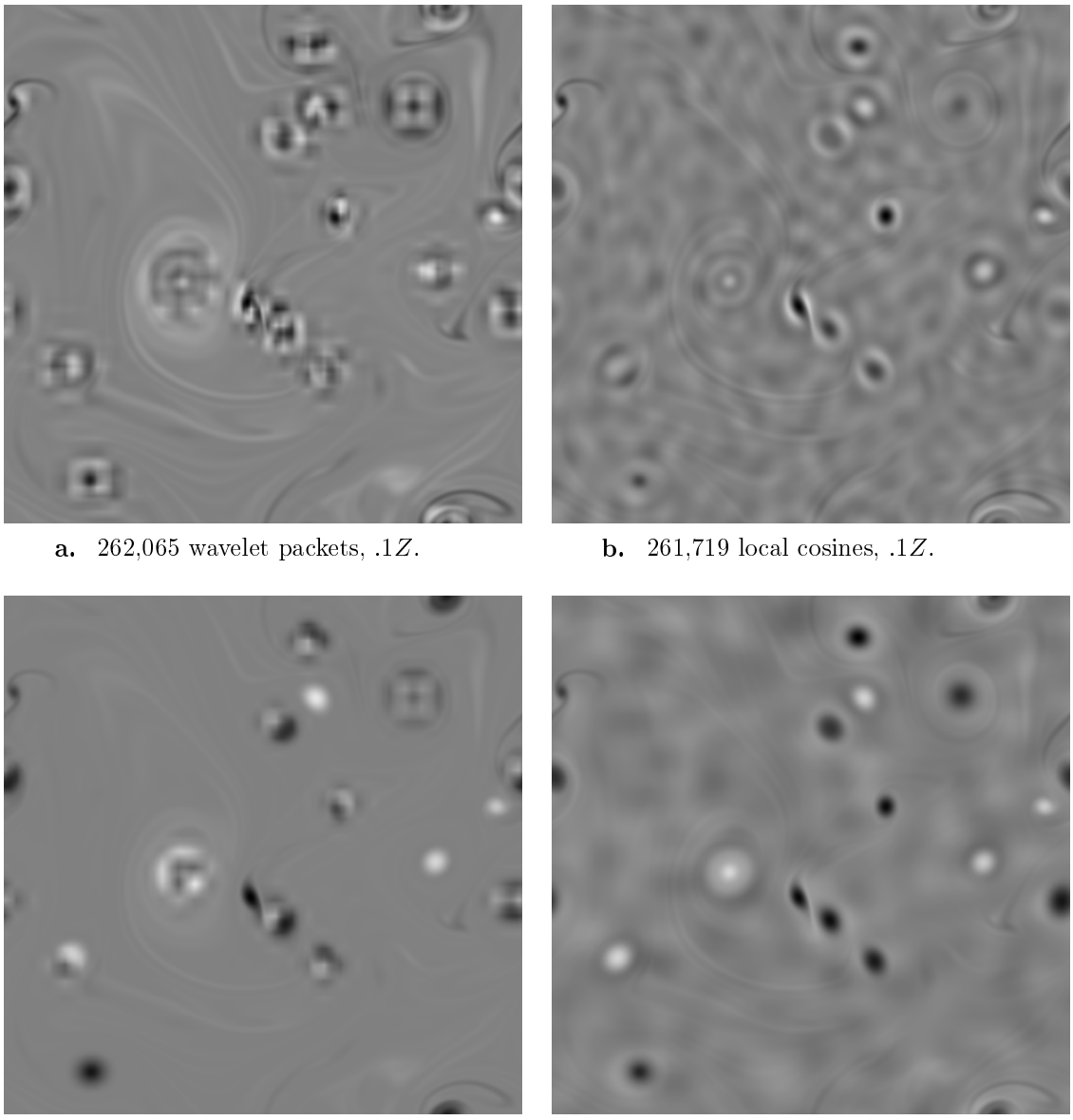

a. 262,065 wavelet packets, $.1Z$.

b. 261,719 local cosines, $.1Z$.

c. 262,128 wavelet packets, $.5Z$.

d. 262,074 local cosines, $.5Z$.

Figure 5: Vorticity fields reconstructed from "many" weakest wavelet packets and local cosines, scaled to fill an 8-bit dynamic range.

The discarded coefficients in both types of compressions will typically contain most of the high frequencies. These are registered at the unsmooth regions of the field, where they must superpose to match the rapid variation. These nonsmooth regions include vortex cores and the strongly sheared regions around vortices, or in between two interacting vortices. Since components are registered around these well localized phenomena, the field reconstructed from the discarded local cosine coefficients can be highly structured, as is evident in Figures 5a–d. At low compression rates such as those of Figures 4a–d, the discarded coefficients constitute a low-enstrophy, homogeneous, noise-like remainder field. Wavelet packets differ from local cosines in this respect chiefly because they are more efficient; they allow more small components to be discarded as noise.

The local cosine components are not isotropic nor even very close to symmetric, since they are tensor products of nonsymmetric one-dimensional functions. We note, however, that we can use symmetric functions if we are willing to using cosines on the odd intervals and sines on the even intervals [3]. Similarly, compactly-supported one-dimensional orthogonal wavelet packets cannot be symmetric or antisymmetric, so they too must give rise to nonisotropic tensor product two-dimensional synthesis functions. However, if we use symmetric biorthogonal filters in the wavelet packet algorithm [20], or still other modifications, we can have compactly-supported synthesis functions which exhibit considerably more symmetry, though they will still have the tensor product character.

3.2 Weak fields reconstructed from the remainders

In both the wavelet packet and local cosine cases, for small compression ratio, the fields reconstructed from discarded weak components are homogeneous, but this homogeneity is lost as the compression ratio increases. At high compression ratios, there are so many components and so much energy in the weak field that it begins to exhibit the same inhomogeneity and anisotropy as the original field.

The requirement that the discarded components look like homogeneous noise imposes an upper limit on the compression ratio. We must not have organized features in the weak component field. The wavelet packet compression permits a higher upper bound than the local cosine compression, since its remainder or weak field remains disorganized up to higher compression ratios.

3.3 Spectra

Figure 6 shows the radial power spectrum of the original vorticity field. Figures 7a–d and 8a–d show the radial power spectra of vorticity fields compressed to varying degrees by both methods. In each plot, three spectra are superposed for comparison: that of the total field, that of the strong components, and that of the weak or discarded components. All plots use the same vertical scale $[6, -10]$, which is the common logarithm of the radial power spectral density, and the

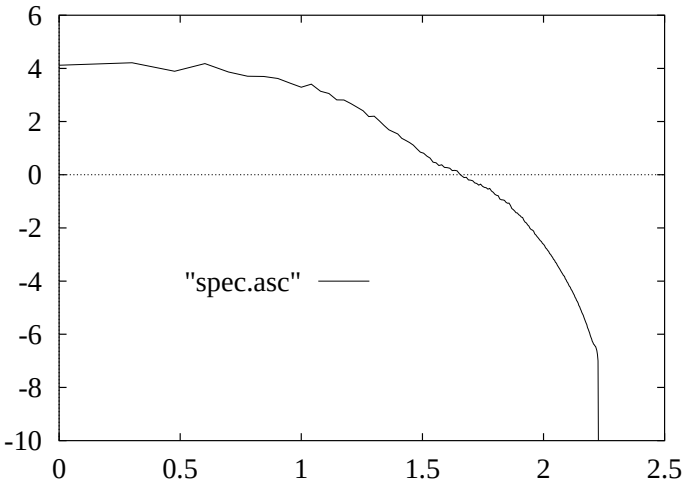

Figure 6: Power spectrum of the original vorticity field.

same horizontal scale $[0, 2.5]$, which is the common logarithm of wavenumber magnitude $|\mathbf{k}|$ and roughly corresponds to the wavenumber range $[0, 316]$. We use uniform scaling in order to allow a fair comparison for both slope and intensity.

The radial power spectra computed from the strong wavelet packets oscillate rather wildly in the large wavenumbers, possibly because of the complicated spectra of individual wavelet packets. There may also be a kind of Gibbs phenomenon, in the wavenumber domain, as the long smooth spectral tails of the wavelet packets try to match the sharp spectral cutoff at $|\mathbf{k}| = 170$ in the original field. The local cosines match this cutoff much better; also, the spectrum of the total field does not oscillate near the cutoff.

We take the inertial region to be the wavenumbers $10 \leq |\mathbf{k}| \leq 50$, or $1.0 \leq |\log_1 0\mathbf{k}| \leq 1.7$. In the inertial region the curve is approximated well by a line of slope -5.63. The radial power spectra of various reconstructions also have identifiable inertial ranges, and we list their slopes in those regions in Table 2. Notice that the local cosine compression's inertial range shrinks much faster than that of the wavelet packet compression, as the absence of discarded high-wavenumber modes eats into the spectrum from the right.

We have listed the slopes of the fields reconstructed from the weakest coefficients in Table 3, looking at the wavenumbers from $|\mathbf{k}| = 1$ up to the highest wavenumber taken to belong to the inertial range. Ideally these slopes would

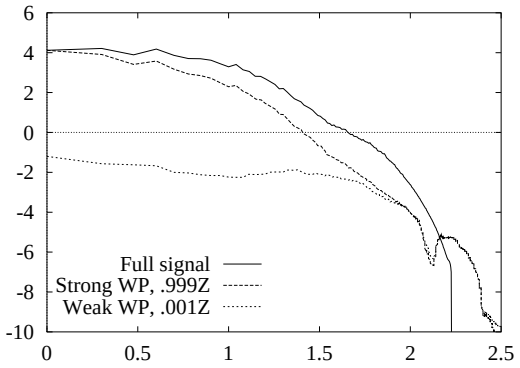

a. 3129 strongest wavelet packets, $.999Z$, plus 259,015 weakest wavelet packets, $.001Z$.

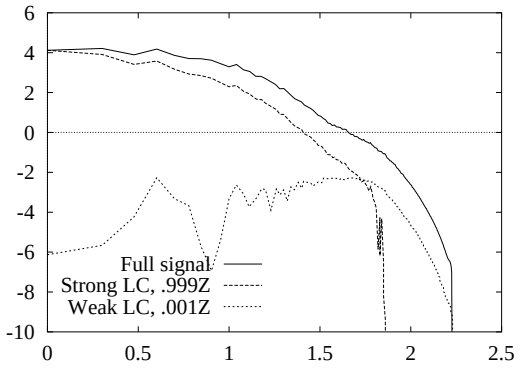

b. 5114 strongest local cosines, $.999Z$, plus 257,030 weakest local cosines, $.001Z$.

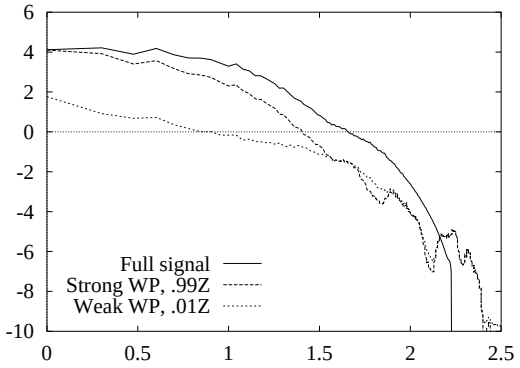

c. 803 strongest wavelet packets, $.99Z$, plus 261,341 weakest wavelet packets, $.01Z$.

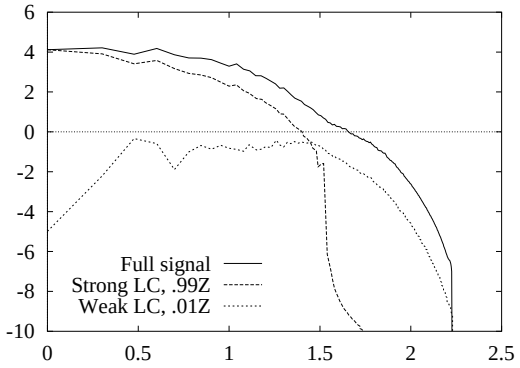

d. 1479 strongest local cosines, $.99Z$, plus 260,665 weakest local cosines, $.01Z$.

Figure 7: Superposed power spectra of the vorticity fields reconstructed from a segmentation into the "many" strongest and "few" weakest wavelet packet and local cosine components.

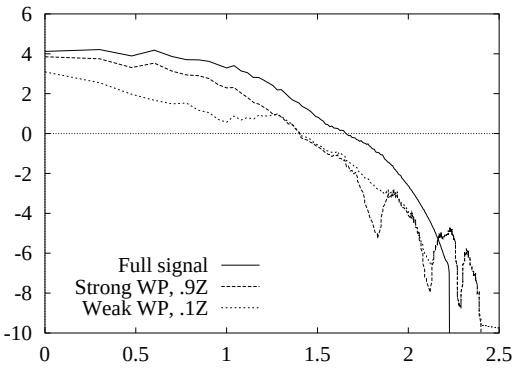

a. 79 strongest wavelet packets, $.9Z$, plus 262,065 weakest wavelet packets, $.1Z$.

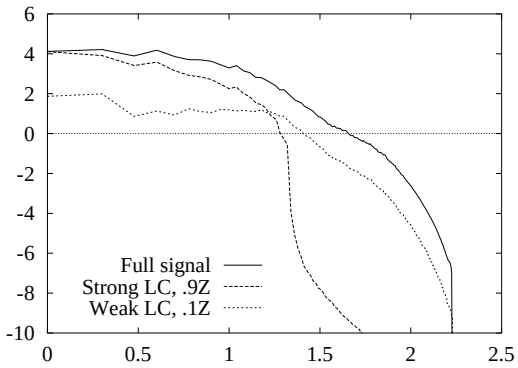

b. 425 strongest local cosines, $.9Z$, plus 261,719 weakest local cosines, $.1Z$.

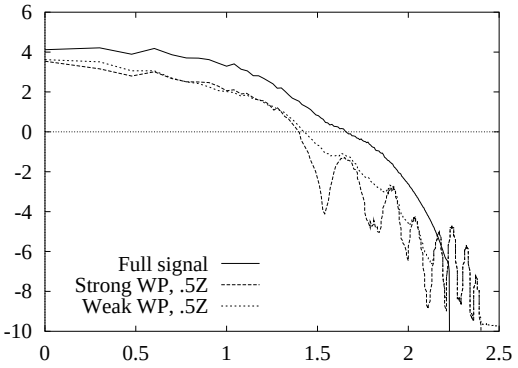

c. 16 strongest wavelet packets, $.5Z$, plus 262,065 weakest wavelet packets, $.5Z$.

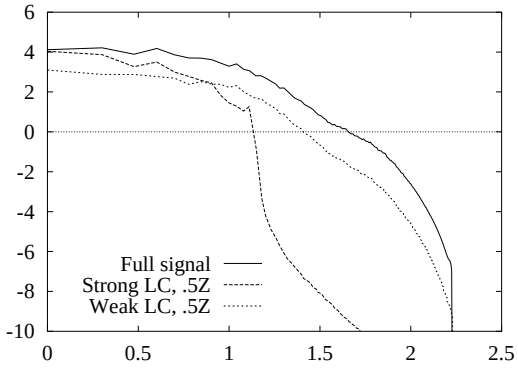

d. 70 strongest local cosines, $.5Z$, plus 262,074 weakest local cosines, $.5Z$.

Figure 8: Superposed power spectra of the vorticity fields reconstructed from a segmentation into the "few" strongest and "many" weakest wavelet packet and local cosine components.

Enstrophy fraction	Wavelet packet inertial range	WP slope	Local cosine inertial range	LC slope
$.999Z$	$[10, 50]$	-6.73	$[10, 50]$	-6.84
$.99Z$	$[10, 50]$	-6.60	$[10, 30]$	-6.99
$.9Z$	$[10, 50]$	-6.26	$[10, 18]$	-6.37
$.5Z$	$[10, 28]$	-6.58	$[8, 12]$	-7.72

Table 2: Spectral slopes in the presumed inertial range of various reconstructions from strong components.

be 0, the radial power spectrum of white noise, but as the compression ratio increases and the discarded coefficients hold more of the enstrophy, they begin to assume more of the spectral characteristics of the original flow.

We can calculate the spectral slopes of the weak wavelet packet reconstructions in Figures 7a,c and 8a,c using rather high wavenumbers, but the weak local cosine spectra are sharply disturbed at the rather low wavenumbers where the strong-field spectrum has its cutoff, as seen in Figures 7b,d and 8b,d. The region where we can estimate the weak-field spectral slope is the chief difference between the two methods. Once that region is chosen, the slope decreases as compression ratio increases at nearly the same rate in both methods.

3.4 Enstrophy concentration

Table 4 shows that wavelet packets concentrate enstrophy better than local cosines, and that the stronger the compression, the better the wavelet packets behave in comparison with local cosines. Wavelet packets are about twice as efficient for retaining 99 and 99.9 percent of the enstrophy, and about five times as efficient for retaining 50 and 90 percent of the enstrophy.

Figure 9 shows the concentration of enstrophy into coefficients in the wavelet packet and local cosine transforms, respectively. The plots represent the enstrophy accumulated by retaining 1, 2, ..., 1000 of the coefficients after sorting them into decreasing order by amplitude. Certainly with the same number of coefficients retained, wavelet packets keep more enstrophy and therefore behave

Enstrophy fraction	Wavelet packet noise-like range	WP slope	Local cosine noise-like range	LC slope
$.001Z$	$[1, 50]$	-0.46	$[1, 50]$	$+2.20$
$.01Z$	$[1, 50]$	-1.92	$[1, 30]$	$+1.68$
$.1Z$	$[1, 50]$	-2.73	$[1, 18]$	-0.53
$.5Z$	$[1, 28]$	-2.70	$[1, 12]$	-0.91

Table 3: Spectral slopes of various reconstructions from weak components.

Enstrophy (percent)	Wavelet packets (per 1000)	Local cosines (per 1000)
99.9	11.94	19.51
99	3.06	5.64
90	0.30	1.62
50	0.06	0.27

Table 4: Fraction of coefficients needed to retain a given portion of the enstrophy in the vorticity field.

better in terms of enstrophy contraction.

3.5 Coherent structure identification

One of our main goals is to locate the centers and influence regions of coherent structures. This is done quite effectively by wavelet packets where the more we compress, the more we isolate strong features. The process of discarding weak wavelet packets kills off the small variations of the vorticity field and leaves only the strongest peaks; Figure 3c shows the culmination of this process, a few surviving vortex cores floating on a perfectly zero background. In the local cosine or any other Fourier-like techniques, the more we compress the smoother the signal will get and the more that quasi-singular features will be smeared one into another. This problem is evident in Figure 3d, but is foreshadowed even even in a moderate compression such as Figure 3b. Another problem with local cosines is the parasitic oscillations we get at high compressions, which interfere with algorithms that localize peaks by finding maxima. In extreme cases, we may even encounter false peaks.

Another of our aims is to identify without ambiguity the dynamic portion of the field and to distinguish it from any passive background. We expect that this background flow should be a kind of noise: spatially homogeneous, isotropic, with a broad spectrum. Ideally, the rejected portion of the field should have amplitudes distributed like independent Gaussian random variables, so it is indistinguishable from measurement error. From the radial spectrum plots in Figures 7a,b, we see that both local cosine and wavelet packet compressions leave remainders that behave much like weak, uncorrelated noise, if the compression ratio stays below 100 or so. As the compresion ratio increases, the noise-like portion of the local cosine spectrum occupies fewer and fewer wavenumbers, until there is virtually no difference betwen the strong and weak spectra. In Figure 8d, the strong and weak spectra match almost perfectly above $|\mathbf{k}| = 12$. By contrast, the noise-like portion of the weak wavelet packet spectrum covers almost the same wavenumbers at low or high compressions, but it gets progressively less noise-like, in the sense of spectral slope, from Figure 7a to Figure 8c.

Both goals advance the efficiency of further computations involving the fields.

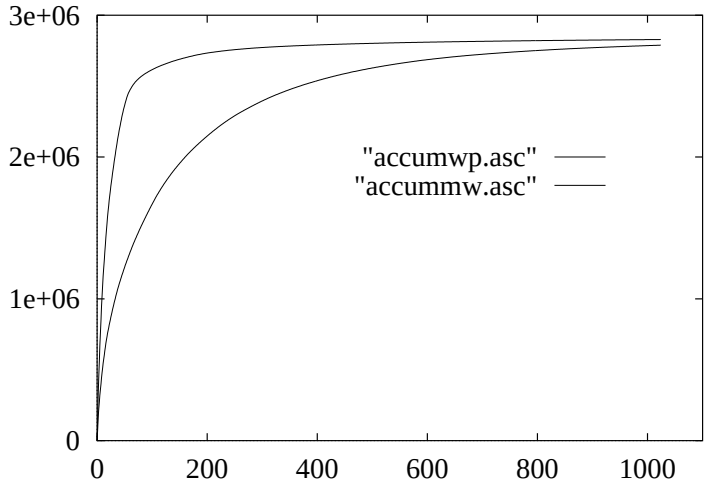

Figure 9: Accumulated enstrophy in partial sums of a decreasing-amplitude rearrangement of wavelet packet and local cosine representations.

When we obtain a satisfactory separation, we can follow the evolution of the two portions separately. We explicitly compute the time evolution of the coherent structures, which costs little because there are few of them. We replace the background by a synthetic noise having the same statistics, i.e, the same spectral slope and similar higher order spectral moments such as skewness and flatness. This model may be simple and cheap to compute. If the background plays only a small role in the evolution, we will obtain reasonably accurate approximations to the "true" evolution at much lower cost.

3.6 Improvements in compression techniques

We may try to do the compression recursively until the discarded coefficients will represent only a noise. Starting with a high compression, we keep the top few strong coefficients. Then we highly recompress the reconstructed remainder field, keeping only the top few strong coefficients, and so on. This is the technique used in *adapted waveform de-noising* [5]. That method introduces a different basis for each stage in the compression so that at the end we do not have a single orthogonal basis representation of the field. However, the resulting "best component" decomposition of the coherent portion of the field can still be evolved by a low complexity computation, while the remainder can be even

more accurately modeled because it has more of the properties of homogeneous noise for a given enstrophy than the remainder produced by a single best basis expansion.

Using the iterative compression technique, we can also try to recover some isotropy by rotating the initial field several times and performing a strong compression at each stage, then superposing all the strong coefficient reconstructed fields. Such methods, however, complicate the problem of computing and comparing the total number of retained coefficients. Further research is needed to circumvent the anisotropy of these separable compressions when the fields to be analyzed are a priori isotropic.

3.7 Conservation of conservation laws

Enstrophy $Z = \|\omega(\cdot,t)\|^2$ is conserved in the Navier–Stokes evolution. We are assured that $Z_{\text{strong}} + Z_{\text{weak}} = Z_{\text{total}}$ for any segmentation $\omega_{\text{total}} = \omega_{\text{strong}} + \omega_{\text{weak}}$ using orthogonal projections, and the conservation law ensures that the total enstrophy in the weak part will never grow more significant.

It is important to note, though, that energy $E = \|\mathbf{u}(\cdot,t)\|^2$ decreases as $t \to \infty$ because of the dissipation term in the Navier–Stokes equation. Having split a vorticity field into pieces, we are not assured that the energy in the two pieces will decay at equal rates. Furthermore, since we are using vorticity and stream function coordinates rather than velocity coordinates, the energy portions E_{strong} and E_{weak} will not add up to E_{total} in a general orthogonal segmentation. Thus it is possible for a significant part of the initial field's energy to wind up in the remainder portion after segmentation, and then for the retained portion's energy to decay faster so that with time the remainder portion's energy becomes even more significant, relatively speaking.

We do have conservation of energy across vorticity segmentations in the Fourier representation, however, where there is a relation $Z = |\mathbf{k}|^2 E$ for the Fourier mode at wavenumber $\mathbf{k}$. Since this holds at all times t, the energy in the remainder field will never grow more significant relative to the retained field. But no such relation holds for wavelet packets or other localized functions. This absence may be a major drawback of our atomic approach, and must be considered seriously if we want to use wavelets or wavelet packets to solve or simulate Navier–Stokes evolutions. Addressing such concerns, however, would go beyond the scope of our present paper.

4 Perspective

Turbulence, either two-dimensional or three-dimensional, seems to be the random superposition of a set of metastable vortices, whose interactions give rise to its characteristic unpredictible behaviour. The goal for modeling or computing the evolution of turbulent flows is to take a coarse-graining point of view,

namely to keep the essential information and discard details as noise.

The bases we have proposed to use in this paper, wavelet packets and local cosines, consist of phase space atoms which can be independently labeled by position, scale, and wavenumber. The Navier-Stokes evolution tends to aggregate these atoms into molecules corresponding to coherent structures. We can calculate the interaction matrix corresponding to the energy and enstrophy cascades in these atomic coordinates, where the number of significant components is much lower.

We gain by drastically reducing the number of degrees of freedom necessary to compute the turbulent flow evolution. Wavelet packets seem to be more efficient than local cosines at accomplishing this reduction. We think that this approach may be extended to the case of three-dimensional turbulent flows, where *vorticity tubes* will play the role of coherent structures. The three-dimensional case poses even greater computing challenges and might benefit even more from parameter reduction than our two-dimensional case.

5 Acknowledgments

The work of the last four authors was supported in part by the European Economic Community program *Human Capital and Mobility*, contract ERB-CHRX-CT92-001, and the NATO program *Collaborative Research*, contract CRG-930456. The first author was supported in part by AFOSR contract F49620-92-J-0106 and NSF grant DMS-9302828.

The vorticity field we use as example in this paper was computed by Thierry Philipovitch using the two-dimensional Navier-Stokes code written by Claude Basdevant. The visualizations were done in collaboration with Jean-François Colonna. These collaborations and grants are gratefully acknowledged.

References

[1] Pascal Auscher, Guido Weiss, and Mladen Victor Wickerhauser. Local sine and cosine bases of Coifman and Meyer and the construction of smooth wavelets. In Charles K. Chui, editor, *Wavelets–A Tutorial in Theory and Applications*, pages 237–256. Academic Press, Boston, 1992.

[2] George K. Batchelor. Computation of the energy spectrum in homogeneous two-dimensional turbulence. *Physics of Fluids*, 12(Supplement II):233–239, 1969.

[3] Ronald R. Coifman and Yves Meyer. Remarques sur l'analyse de Fourier à fenêtre. *Comptes Rendus de l'Académie des Sciences de Paris*, 312:259–261, 1991.

[4] Ronald R. Coifman, Yves Meyer, Stephen R. Quake, and Mladen Victor Wickerhauser. Signal processing and compression with wavelet packets. In Yves Meyer and Sylvie Roques, editors, *Progress in Wavelet Analysis and Applications*, Proceedings of the International Conference "Wavelets and Applications," Toulouse, France, 8–13 June 1992, pages 77–93. Editions Frontieres, Gif-sur-Yvette, France, 1993.

[5] Ronald R. Coifman and Mladen Victor Wickerhauser. Wavelets and adapted waveform analysis. In John J. Benedetto and Michael Frazier, editors, *Wavelets: Mathematics and Applications*, Studies in Advanced Mathematics, pages 399–423. CRC Press, Boca Raton, Florida, 1992.

[6] Ingrid Daubechies. Orthonormal bases of compactly supported wavelets. *Communications on Pure and Applied Mathematics*, XLI:909–996, 1988.

[7] Marie Farge, Eric Goirand, Yves Meyer, Frédéric Pascal, and Mladen Victor Wickerhauser. Improved predictability of two-dimensional turbulent flows using wavelet packet compression. *Fluid Dynamics Research*, 10:229–250, 1992.

[8] Dennis Gabor. Theory of communication. *Journal of the Institute of Electrical Engineers*, 93(III):429–457, 1946.

[9] A. N. Kolmogorov. On degeneration of isotropic turbulence in an incompressible viscous liquid. *Doklady Akademii Nauk SSSR*, 31:538–540, 1941. In Russian.

[10] Robert H. Kraichnan. Inertial ranges in two-dimensional turbulence. *Physics of Fluids*, 10:1417–1423, 1967.

[11] Robert H. Kraichnan. Statistical dynamics of two-dimensional flow. *Journal of Fluid Mechanics*, 67, part 1:155–175, 1975.

[12] Robert H. Kraichnan and D. Montgomery. Two-dimensional turbulence. *Report on Progress in Physics*, 43:547, 1980.

[13] Stéphane G. Mallat. A theory for multiresolution signal decomposition: The wavelet decomposition. *IEEE Transactions on Pattern Analysis and Machine Intelligence*, 11:674–693, 1989.

[14] Henrique Malvar. Lapped transforms for efficient transform/subband coding. *IEEE Transactions on Acoustics, Speech, and Signal Processing*, 38:969–978, 1990.

[15] C. Marchioro and M. Pulvirenti. *Vortex Methods in 2D Fluid Dynamics*. Number 203 in Lecture Notes in Physics. Springer-Verlag, Berlin, 1984.

[16] Yves Meyer. Orthonormal wavelets. In Jean-Michel Combes, Alexander Grossmann, and Philippe Tchamitchian, editors, *Wavelets: Time-Frequency Methods and Phase Space*, pages 21–37. Springer-Verlag, Berlin, second edition, 1989.

[17] Andrei Sergeevich Monin and A. M. Yaglom. *Statistical Fluid Mechanics; Mechanics of Turbulence*. MIT Press, Cambridge, Massachusetts, 1971. Edited by John L. Lumley.

[18] Philip Saffman. Vortex interactions and coherent structures in turbulence. In R. E. Meyer, editor, *Transition and Turbulence*. Academic Press, 1981.

[19] Mladen Victor Wickerhauser. High-resolution still picture compression. *Digital Signal Processing: a Review Journal*, 2(4):204–226, October 1992.

[20] Mladen Victor Wickerhauser. *Adapted Wavelet Analysis from Theory to Software*. AK Peters, Ltd., Wellesley, Massachusetts, 9 May 1994. 486+xii pages, with diskette. To appear.

[21] Mladen Victor Wickerhauser. Comparison of picture compression methods: Wavelet, wavelet packet, and local cosine transform coding. In Charles K. Chui, editor, *Wavelets: Theory, Algorithms, and Applications*, Proceedings of the International Conference in Taormina, Sicily, 14–20 October 1993. Academic Press, San Diego, California, 1994. To appear.

[22] G. S. Winckelmans and A. Leonard. Contributions to vortex particle methods for the computation of three-dimensional incompressible unsteady flows. *Journal of Computational Physics*, 109:247–273, 1993.